Electrochemistry Communications 105 (2019) 106491

Contents lists available at ScienceDirect

Electrochemistry Communications

journal homepage: www.elsevier.com/locate/elecom

Full communication

A high-performance solid-state synthesized $LiVOPO_4$ for lithium-ion batteries

Yong Shi[a], Hui Zhou[a], Sylvia Britto[d,b], Ieuan D. Seymour[d,b], Kamila M. Wiaderek[c,b], Fredrick Omenya[a], Natasha A. Chernova[b], Karena W. Chapman[b,c,e,1], Clare P. Grey[d,b], M. Stanley Whittingham[a,b,*]

[a] Chemistry and Materials Science and Engineering, Binghamton University, Binghamton, NY 13902, United States
[b] NorthEast Center for Chemical Energy Storage (NECCES), Binghamton, NY 13902, United States
[c] X-ray Science Division, Advanced Photon Source, Argonne National Laboratory, Argonne, IL 60439, United States
[d] Department of Chemistry, University of Cambridge, Lensfield Road, Cambridge CB2 1EW, United Kingdom
[e] Department of Chemistry, Stony Brook University, Stony Brook, NY 11974, United States

ARTICLE INFO

Keywords:
Li-ion battery
Cathode
Annealing
Structural disorder

ABSTRACT

ε-$LiVOPO_4$, a multi-electron cathode material for Li-ion batteries, suffers from structural disorder upon nano-sizing by high-energy ball-milling, which impedes kinetics and promotes undesirable interfacial side reactions. This work presents a feasible way to decrease the disorder in the ball-milled composite of ε-$LiVOPO_4$/C by post-annealing at 450 °C in an Ar atmosphere, with no reduction reaction caused by carbon and no particle growth. The post-annealed material shows recovered voltage plateaus, enhanced kinetics of Li diffusivity, and suppressed interfacial reactions. As a result, a high-performance solid-state synthesized ε-$LiVOPO_4$ can be obtained, delivering a capacity of 270 mAh g^{-1} at C/5 with less than 4% degradation upon 100 cycles.

1. Introduction

Lithium-ion batteries (LIBs) have advanced significantly since their introduction in the 1970s [1–3]. In the last decade, rapidly growing electric vehicles market has placed increased demand for high energy density LIBs [4,5]. To meet this demand, cathode materials with energy density of at least 800 Wh kg^{-1} are required [5]. A multi-electron cathode material, triclinic ε-$LiVOPO_4$, is considered to be one of the most promising candidates. ε-$LiVOPO_4$ can provide two redox transitions, V^{5+}/V^{4+} and V^{4+}/V^{3+}, at 4 V and 2.5 V, respectively, resulting in a capacity of 305 mAh g^{-1} (1C = 153 mAh g^{-1}) and an energy density over 900 Wh kg^{-1} [2,3].

However, the poor electronic and ionic conductivities of ε-$LiVOPO_4$ limit its application. To overcome these challenges, a variety of synthesis methods have been explored. Harrison et al. [6] synthesized ε-$LiVOPO_4$ with particle sizes ranging from 100 nm to a few microns by microwave-solvothermal method. Hollow ε-$LiVOPO_4$ was synthesized by Ren et al. [7] *via* a hydrothermal method and by Saravanan et al. [8] using solvothermal approach. These materials were tested in a high-voltage range of 3 to 4.5 V and attained capacities varying from 90 to 130 mAh g^{-1} at moderate current densities. Zhou et al. [9] obtained ε-$LiVOPO_4$ through sol-gel method at 400 and 700 °C. The 400 °C sample showed better electrochemical performance in the 1.6–4.5 V range due to its smaller particle size and the conducting carbon residue. Kerr et al. [10] reported a delithiated form, ε-$VOPO_4$, with particle size of 0.6–0.75 μm formed by heating hydrothermally synthesized H_2VOPO_4. The capacity over 100 mAh g^{-1} was achieved for up to 100 cycles at C/10 over 3.0–4.5 V range. Our group investigated the possibility of two Li cycling in this material [11,12] and most recently have demonstrated a fully reversible intercalation of two Li-ions in ε-$VOPO_4$ through control of the morphology and particle size (200 nm) of the hydrothermally synthesized H_2VOPO_4 [13]. The full theoretical capacity of 305 mAh g^{-1} was delivered at C/25 in 1.6 V–4.5 V range for at least 50 cycles. It was attributed to nano-size and good crystallinity of this material, combined with thorough carbon coating [13].

Solid-state reaction is an effective method to prepare highly crystalline ε-$LiVOPO_4$ [14–17]. However, similarly to $LiFePO_4$, to achieve small particle size and a good electronic conductive network [18–21], leading to capacities close to the theoretical, ε-$LiVOPO_4$ has to be high-energy ball-milled with carbon [22]. Our earlier work pointed out that

* Corresponding author at: Chemistry and Materials Science and Engineering, Binghamton University, Binghamton, NY 13902, United States.
E-mail address: stanwhit@gmail.com (M.S. Whittingham).
[1] Now at the Department of Chemistry, Stony Brook University, Stony Brook, NY 11974, USA.

https://doi.org/10.1016/j.elecom.2019.106491
Received 11 June 2019; Received in revised form 30 June 2019; Accepted 1 July 2019
Available online 02 July 2019

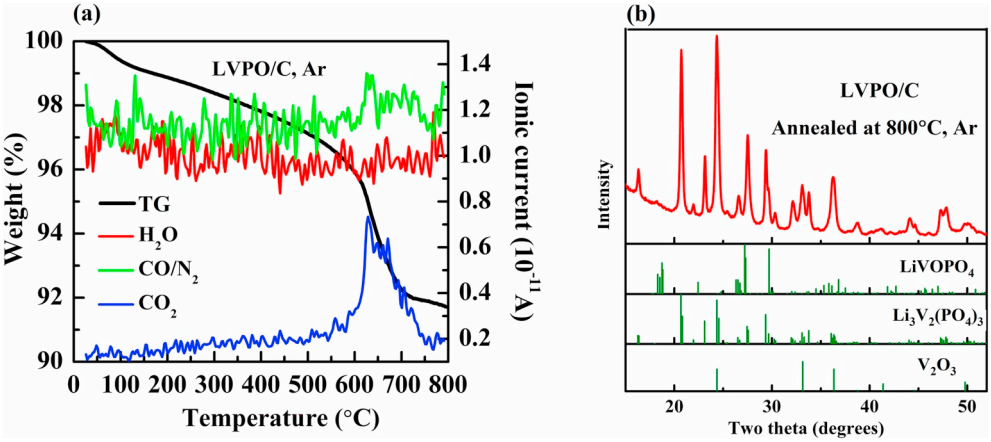

Fig. 1. (a) TG-MS measurements of the ball-milled LVPO/C composite in Ar atmosphere. (b) XRD pattern of the products obtained at 800 °C in the TG-MS test.

ball-milling induces disorder in ε-$LiVOPO_4$ bulk, which impedes kinetics and promotes significant interfacial side reactions, causing polarization and energy loss [22,23].

In this work, we employ annealing treatment of the ball-milled ε-$LiVOPO_4$/C composite in order to decrease the bulk disorder. The challenge of this approach is to keep the particle size small and to prevent vanadium reduction by carbon upon annealing. We successfully used thermogravimetric analysis to optimize the annealing temperature; X-ray diffraction (XRD), pair distribution function analysis (PDF), solid-state ^{7}Li and ^{31}P NMR, along with scanning electron microscopies were used to study the structural and morphological properties of the post-annealed ε-$LiVOPO_4$. The electrochemical results highlight the importance of reducing disorder in ε-$LiVOPO_4$ to achieve a high-performance ε-$LiVOPO_4$.

2. Experimental methods

ε-$LiVOPO_4$ (LVPO) was synthesized by a solid-state method (see Supporting Information for details) [22]. As-prepared LVPO was high-energy ball-milled (SPEX, 8000D) with graphene nanoplatelets (xGnP-C750) for 0.8 h, giving the disordered LVPO (D-LVPO). D-LVPO was then post-annealed in argon atmosphere to produce LVPO with reduced disorder in bulk (rD-LVPO). X-ray diffraction (XRD) tests were carried out on Bruker D8 ADVANCE diffractometer with Cu Kα radiation. The crystallite size and strain effects were analyzed from the peak broadening using the Double-Voigt approach in TOPAS, yielding volume weighted mean crystallite sizes (domain sizes) $L_{Vol\text{-}IB}$ and a mean strain value e_0 [24]. The scattering data for the pair distribution function (PDF) analysis were collected at beamline 11-ID-B at the Advanced Photon Source, Argonne National Laboratory. High energy X-rays (58.26 keV, λ = 0.2128 Å) were combined with a large amorphous silicon-based area detector (Perkin–Elmer) to collect data to Q_{max} = 24 Å^{-1} [25–27]. The data were integrated using GSAS-II [28] using a CeO_2 standard (SRM674b) as a calibrant. The large Q-range total scattering data were corrected and Fourier transformed to get $G(r)$, the PDF within pdfgetX3 [29]. Structure models were refined against the PDF data within PDFgui [30]. Thermogravimetric analysis (TGA) and gas evolution were examined by TGA equipped with mass spectrometry (MS) (TG 209 F1 Iris, Netzsch). Samples were loaded in an alumina crucible and heated up to 800 °C under Ar flow at a heating rate of 5 °C/min. The solid-state ^{7}Li and ^{31}P NMR spectra were acquired on a 4.7 T (200 MHz) Bruker Avance III wide bore magnet at Larmor frequencies of 77.775 and 81.176 MHz respectively. All the experiments were carried out with a Bruker 1.3 mm MAS probe spinning at frequency of 60 kHz. A rotor synchronized, spin-echo pulse sequence was used for ^{7}Li, with a π/2 pulse length of 1.02 μs at a power of 43.5 W, set on an external reference of Li_2CO_3 (referenced to 1.1 ppm). A rotor synchronized, spin-echo pulse sequence was also used for ^{31}P with a π/2 pulse length of 0.98 μs at a power of 53 W, set on an external reference of adenosine diphosphate (referenced to 1 ppm). Scanning electron microscopy (SEM) was performed on a Zeiss Supra 55VP microscope. The ball-milled composite LVPO/graphene nanoplatelets was mixed with poly(vinylidene difluoride) (75:15:10 wt%) to make the slurry. The slurry was then cast on Al foil and dried at 80 °C in a vacuum oven overnight. The loading of active material is 2–4 mg cm^{-2}. The electrodes were assembled into 2325-type coin cells with a Li metal chip as anode and 1 M $LiPF_6$ in EC/DMC (EC/DMC = 1:1) as electrolyte. Electrochemical tests were performed on VMP multichannel potentiostats (Bio-Logic) in a voltage range 1.6 to 4.5 V to ensure two Li cycling. Cyclic voltammetry (CV) tests were carried out at a variety of scanning rates from 0.02 to 0.3 mV s^{-1}. The details of *in-situ* EIS are presented in SI (Fig. S1).

3. Results and discussion

One possible drawback of annealing ε-$LiVOPO_4$ (LVPO) in the presence of carbon is the possibility of a reduction reaction. To reveal the temperature of this reduction process, a TG-MS test of LVPO ball-milled with carbon was carried out in argon atmosphere (Fig. 1(a)). The TG-MS data shows a weight loss associated with carbon dioxide generation above 500 °C. The XRD pattern of the final products obtained at 800 °C (Fig. 1(b)) reveals a mixture of $Li_3V_2(PO_4)_3$ and V_2O_3. The valence state of vanadium in both products is V^{3+}, which proves that V^{4+} was reduced by carbon at the elevated temperatures. Based on these results, the following reduction reaction occurs above 500 °C:

$$12LiVOPO_4 + 3C \rightarrow 4Li_3V_2(PO_4)_3 + 2V_2O_3 + 3CO_2 \quad (1)$$

The theoretical weight loss due to CO_2 formation is 6.4%, which is close to the observed of ~8% weight loss. Extra 1.6% loss may be attributed to the surface water and oxygen absorbed in the sample leading to more carbon burning out. To avoid this reduction reaction, a temperature of 450 °C was chosen to post-anneal the ball-milled LVPO/C composite.

The XRD patterns of disordered D-LVPO and post-annealed rD-LVPO are presented in Fig. 2(a). Both materials are phase-pure with sharper diffraction peaks observed for rD-LVPO. The mean crystallite sizes (domain sizes) $L_{Vol\text{-}IB}$ calculated by the Double-Voigt approach on TOPAS [24] are ~30 nm for both D-LVPO and rD-LVPO, indicating that the primary crystallite size did not change upon post-annealing. A smaller strain e_0, however, was observed in rD-LVPO, which explains the sharpness of the XRD peaks. It is consistent with the idea that strain can be reduced upon post-annealing, as increased diffusion at elevated temperatures likely leads to the healing of disorder and other structural defects. In addition, the secondary particle size of rD-LVPO is similar to

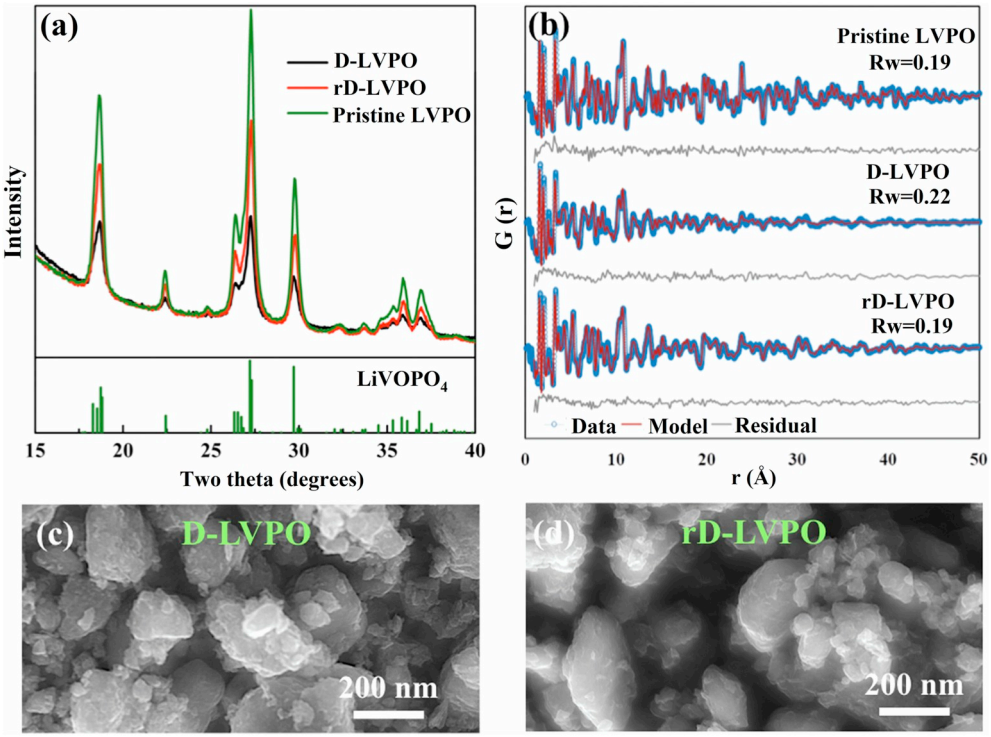

Fig. 2. (a) XRD patterns, (b) pair distribution function (PDF) analysis, (c) SEM of D-LVPO and (d) of rD-LVPO.

that of D-LVPO, ~200 nm, as shown in the SEM images (Fig. 2(c–d)), indicating that small particles did not coalesce upon post-annealing.

To further understand the effect of annealing on the structure of D-LVPO, the structure coherence of D-LVPO and rD-LVPO was analyzed from the PDF data (Fig. 2(b)) and compared to that of as-synthesized LVPO reference. All the three samples fit well with the triclinic ε-$LiVOPO_4$ phase (the lattice parameters are summarized in Table S1). For D-LVPO, the structural coherence is 4.2 nm, which is smaller than the primary crystallite size aforementioned, suggesting that the particle ordering does not extend beyond ~7 unit cells. For rD-LVPO, structural coherence increases to 7.3 nm and V thermal parameters are significantly reduced (Table S2). This result confirms the decrease of structural disorder in rD-LVPO.

Solid-state ^{7}Li and ^{31}P NMR studies were also carried out to further understand the structure of rD-LVPO. The pristine LVPO exhibits a single isotropic ^{7}Li NMR resonance at ~77 ppm (Fig. 3(a)) [22]. This is consistent with hybrid DFT calculations which predict Fermi contact shifts of 76–91 ppm and 63–75 ppm for the two Li sites, Li1 and Li2, present in the ε-$LiVOPO_4$ structure. The single peak observed experimentally can be assigned to an overlap of the Li1 and Li2 shifts. In the disordered structure, in addition to the 77 ppm peak (peak 1) a broad peak at ~0 ppm (peak 2) is observed (Fig. 3(b)). In rD-LVPO, the ratio of the intensities of the 77 ppm peak to the 0 ppm peak increases compared to D-LVPO (Fig. 3(c)). Deconvolution of the ^{7}Li NMR peaks gives a clearer indication of the various local environments in the samples. Deconvolution of the NMR spectrum of the D-LVPO indicates that it contains a broad resonance at ~49 ppm (peak 3) in addition to the peaks at ~77 ppm and ~0 ppm, indicative of a distribution of Li environments. Both the peaks that are not seen in the pristine sample (~0 ppm and ~49 ppm) are characteristic of local disorder in the structure, corresponding to a disordering of the Li1 and Li2 sites in the two 1D channels along the [110] direction in the structure [22]. Our earlier work has shown that a disordered model which corresponds to Li sites being equivalent in the two tunnels gives rise to calculated hyperfine shifts of 18–22 ppm and 37–55 ppm which are close to the experimentally observed shifts of ~0 ppm and 49 ppm respectively [22]. Disappearance of the broad peak at ~49 ppm in the rD-LVPO sample clearly indicates that the local disorder of the Li ions has decreased. The ^{31}P NMR spectra show more pronounced indications of less disorder in rD-LVPO. Pristine ε-$LiVOPO_4$ contains two isotropic resonances at 1650 ppm (peak 1′) and 1458 ppm (peak 2′) consistent with the two crystallographically distinct P sites in the ε-$LiVOPO_4$ structure (Fig. 3(d)) [22]. Deconvolution of the ^{31}P spectrum of D-LVPO (Fig. 3(e)) suggests that, similar to ^{7}Li spectrum, in addition to two peaks of the pristine sample there is a broad resonance centred at 2653 ppm (peak 3′), which disappears in rD-LVPO (Fig. 3(f)). Again, the observed broad resonance is attributed to a disordering of the Li ions [22]. This broad resonance disappears in the rD-LVPO sample, indicating that the reordering of Li ions occurs, consistent with the ^{7}Li NMR.

The electrochemical tests were conducted to examine the effect of reduced disorder on the electrochemistry of the post-annealed LVPO. The D-LVPO and rD-LVPO were discharged to 1.6 V first then charged back to 4.5 V. The full charge/discharge curves at a reaction rate of C/10 (0.038 mA cm^{-2}) are shown in Fig. 4(a). In D-LVPO, the voltage plateaus caused by two-phase reactions at 4 V ($VOPO_4$ ↔ $LiVOPO_4$) and below 3 V ($LiVOPO_4$ ↔ $Li_{1.5}VOPO_4$ ↔ $Li_{1.75}VOPO_4$ ↔ Li_2VOPO_4) [12,16,17] are absent, resulting in a sloping potential profile with a capacity of 196 mAh g^{-1}. The annealed rD-LVPO, however, shows pronounced plateaus at all voltage windows, delivering a higher discharge capacity compared to D-LVPO. Also, the voltage hysteresis is greatly decreased in the annealed material compared to that of D-LVPO. The sample rD-LVPO also presents an excellent cycling stability (Fig. 4(c)). At C/5, D-LVPO has an initial capacity of 155 mAh g^{-1} with only 20 mAh g^{-1} remained over 100 cycles and all the voltage plateaus are vanished (Fig. 4(d)). On the contrary, each of the voltage plateaus of rD-LVPO is clearly distinguishable after 100 cycles (Fig. 4(e)). rD-LVPO delivers an initial capacity of 270 mAh g^{-1} with less than 4% capacity loss over 100 cycles at C/5. In addition, compared to D-LVPO, the growth of interfacial resistance upon extensive cycling is greatly suppressed in rD-LVPO, as depicted in impedance spectra (insets of Fig. 4(d) and (e)). Moreover, sample rD-LVPO has higher discharge

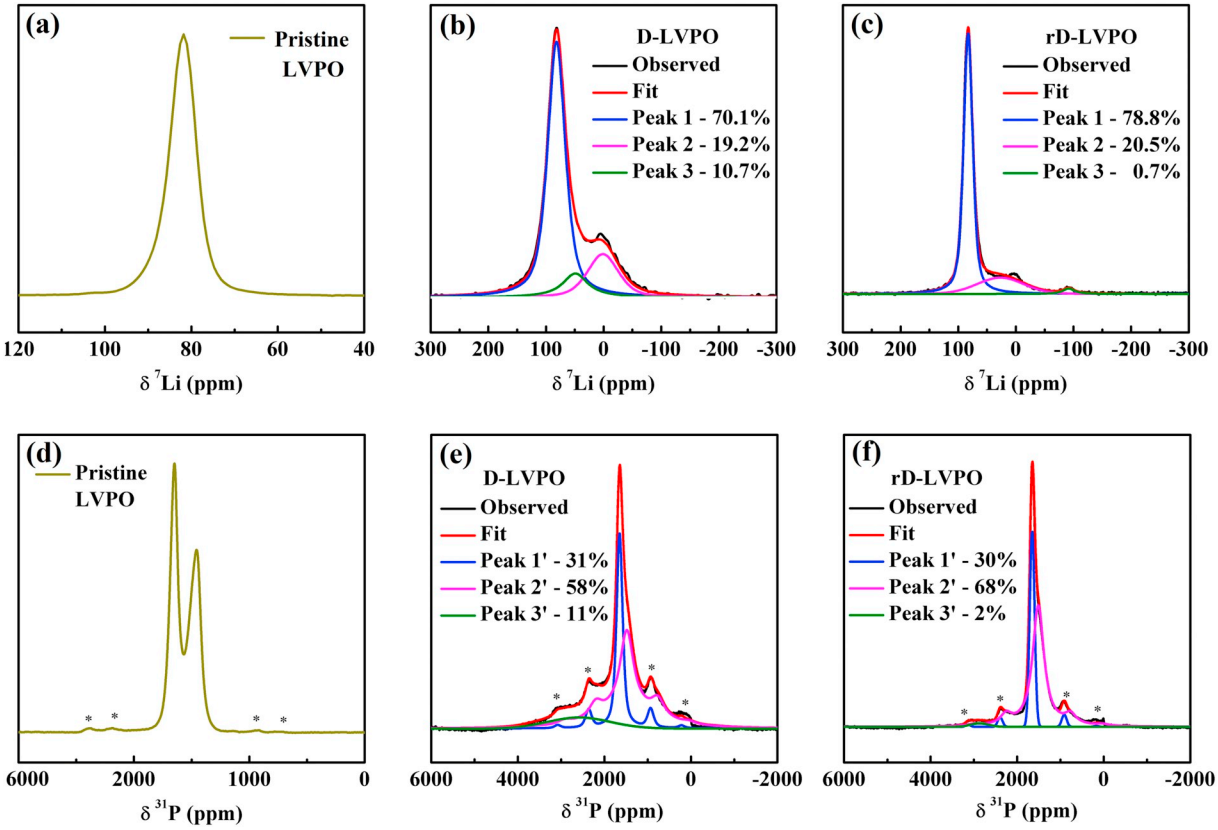

Fig. 3. (a) ^{7}Li NMR spectra of the pristine LVPO acquired at 60 kHz spinning frequency at a field of 4.7 T; deconvolution of ^{7}Li NMR spectrum of (b) D-LVPO and (c) rD-LVPO. The spectra are fitted with two Lorentzian (peak 1 and peak 2) and 1 Gaussian (peak 3) peaks. Only the isotropic region is shown. (d) ^{31}P NMR spectra of the pristine LVPO acquired at 60 KHz spinning frequency at an external field of 4.7 T; deconvolution of ^{31}P NMR spectrum of (e) D-LVPO and (f) rD-LVPO. The spectra are fitted with three Gaussian peaks. Spinning sidebands are marked by asterisks (*).

capacities at all the reaction rates as shown in Figs. 4(b) and S2. It is noteworthy that the capacity of D-LVPO is restored when the rate is reduced back to C/10, suggesting that the decrease of capacity at high rate in the disordered structure is a result of the kinetics issue instead of the degradation of active materials during cycling.

Cyclic voltammograms were carried out to study the kinetics in rD-LVPO. Fig. 4(f) depicts the CV profiles of both samples at a scan rate of 0.02 mV s^{-1}. Sample rD-LVPO displays more sharp and symmetric anodic/cathodic peaks compared to D-LVPO, indicating more pronounced two-phase transitions between Li_xVOPO_4 (x = 2, 1.75, 1.5, 1 and 0). This result is consistent with the observation of the restored voltage plateaus in the charge/discharge profiles aforementioned. The peak potential differences ($\Delta E_p = \Delta E_{pa} - \Delta E_{pc}$) in rD-LVPO presents a smaller value than those of D-LVPO (Table S3), consistent with the smaller hysteresis observed in the charge/discharge profiles, which suggests an improved reversibility of the electrochemical reaction. Fig. 4(g) compares the CV curves of D-LVPO and rD-LVPO measured at different scan rates from 0.02 to 0.30 mV s^{-1}. Of note the potential peaks of D-LVPO shift farther apart and gradually merge into one broad peak with increasing scan rate. In contrast, rD-LVPO displays distinct anodic/cathodic peaks and narrow peak separations with increasing scan rate, again, indicating an improved kinetics [31,32]. The apparent chemical diffusion coefficient of Li ions in rD-LVPO determined using the Randles–Sevcik equation (see SI and Fig. S3 for details) is 3.9×10^{-11} cm^2 s^{-1}, one order of magnitude higher than that of D-LVPO with the value of 4.0×10^{-12} cm^2 s^{-1}. The CV results reveal the improved kinetics of Li diffusivity in the more ordered LVPO structure, which contributes to the superior rate capability of rD-LVPO.

We have also shown previously, that ε-Li_xVOPO_4 is likely to be pseudo-1D ionic conductor, where the capacity in the high-voltage region is limited by Li mobility [17]. The ball-milling of LVPO introduces disorder that impedes Li-ion kinetics, and promotes significant interfacial side reactions, causing polarization and energy loss [22,23]. The significant decrease of disorder upon post-annealing, as evidenced by the PDF and NMR data, can improve Li mobility, causing the improved electrochemistry of rD-LVPO. In the disordered structure D-LVPO, the voltage changes continuously in a wide range as Li ions are removed from various disordered sites with nonequivalent site energy [17,22,33]. In rD-LVPO, however, the ordered Li sites are reconstructed, leading to stable voltage plateaus. Interestingly, post-annealing also suppresses interfacial resistance, as demonstrated in the CV and EIS results. Thus, rD-LVPO has a reduced polarization, giving the superior rate capability and stable cyclability compared to D-LVPO. Overall, the utilization of the energy in LVPO is significantly enhanced.

4. Conclusions

This work highlights the importance of removing the disorder in the solid-state synthesized ε-$LiVOPO_4$ caused by ball-milling during nano-sizing. We have shown a facile method to reduce the disorder by post-annealing the ball-milled composite of ε-$LiVOPO_4$/C at 450 °C in Ar atmosphere. Under these conditions, ε-$LiVOPO_4$ is not reduced by carbon, the structural disorder is alleviated, and the small particle size is retained. Upon post-annealing, the voltage plateaus due to the two-

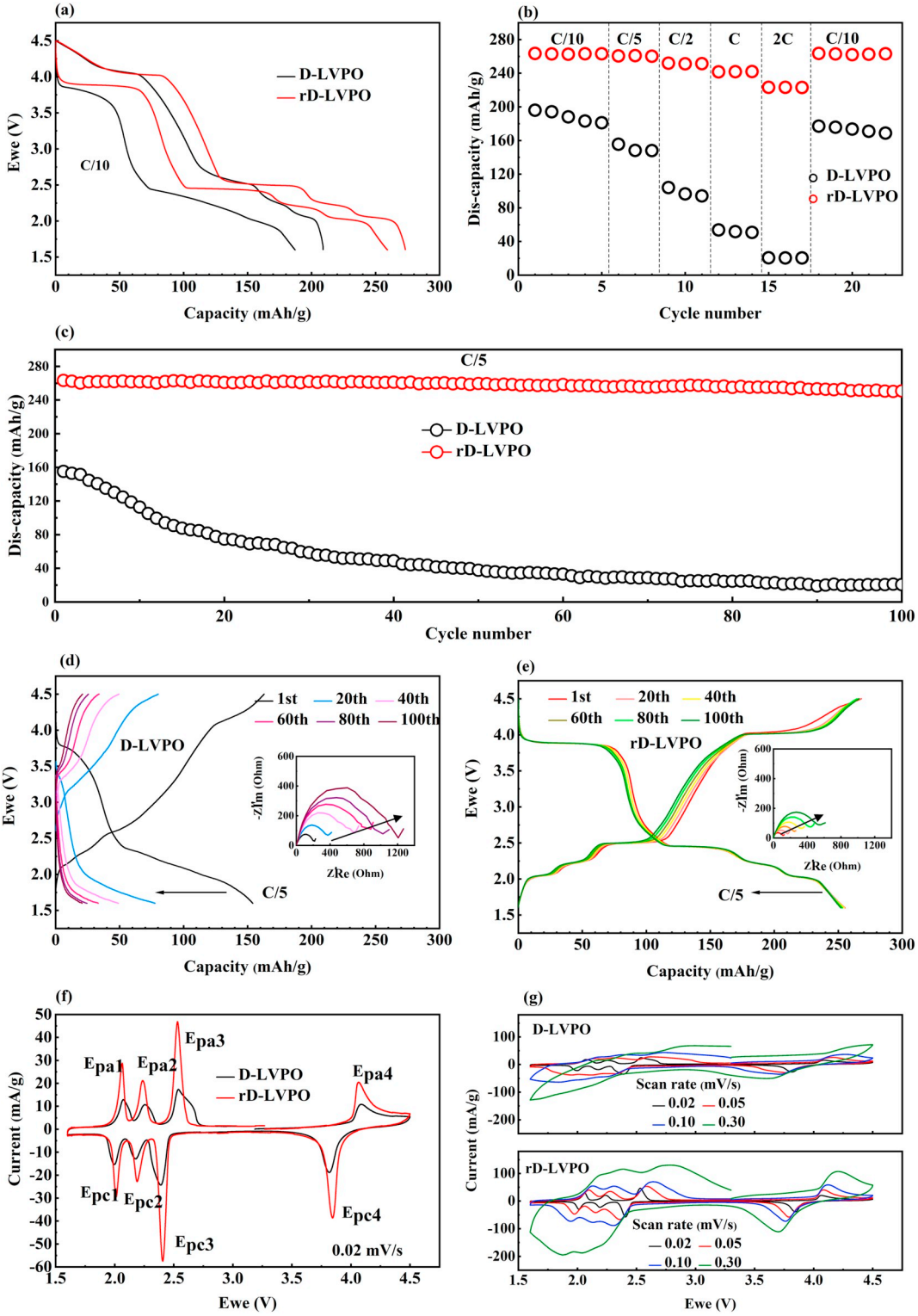

Fig. 4. (a) The charge/discharge curves at the first full cycle at C/10, (b) the rate capability, and (c) the cycling performance at C/5 of D-LVPO and rD-LVPO. The charge/discharge profiles for every twenty cycles at C/5 with *in-situ* impedance spectra (inset) of (d) D-LVPO and (e) rD-LVPO. Cyclic voltammograms of D-LVPO and rD-LVPO (f) with a scan rate of 0.02 mV s^{-1} and (g) with scan rate from 0.02 mV s^{-1} to 0.30 mV s^{-1}.

phase reactions are recovered, the kinetics of Li diffusivity is improved, and the interfacial reactions are suppressed. As a result, polarization is greatly reduced, and a high-performance ε-$LiVOPO_4$ is obtained in terms of capacity, rate capability, and cyclability. Our results show that the post-annealed ε-$LiVOPO_4$ has a capacity of 270 mAh g^{-1} at C/5 (0.076 mA cm^{-2}) with less than 4% degradation upon 100 cycles.

Declaration of Competing Interest

The authors declare no competing financial interest.

Acknowledgments

This research was funded by U.S. Department of Energy, Office of Energy Efficiency and Renewable Energy (EERE) program under BMR award no. DE-EE0006852. The structural characterization using NMR and PDF techniques was supported by the NorthEast Center for Chemical Energy Storage (NECCES), an Energy Frontier Research Center supported by the U.S. Department of Energy, Office of Science, Office of Basic Energy Sciences under award no. DE-SC0012583. This research used resources of the Advanced Photon Source, a U.S. Department of Energy (DOE) Office of Science User Facility operated for the DOE Office of Science by Argonne National Laboratory under Contract No. DE-AC02-06CH11357. We thank Dr. Fengxia Xin for help with TG-MS data acquisition, and Drs. Jatinkumar Rana and Jia Ding, for many helpful discussions.

Appendix A. Supplementary data

The equivalent circuit model for the impedance spectra; lattice and thermal parameters obtained from the PDF tests of pristine LVPO, D-LVPO, and rD-LVPO; voltage differences of cathodic peaks and anionic peaks in CV tests for D-LVPO and rD-LVPO; cycling curves at different rates; and the linear regression plot of i_p *vs.* $v^{1/2}$ obtained from the CV tests. Supplementary data to this article can be found online at https://doi.org/10.1016/j.elecom.2019.106491.

References

[1] M.S. Whittingham, Science 192 (1976) 1126–1127.
[2] M.S. Whittingham, Chem. Rev. 114 (2014) 11414–11443.
[3] M.S. Whittingham, Chem. Rev. 104 (2004) 4271–4302.
[4] B. Nykvist, F. Sprei, M. Nilsson, Energy Policy 124 (2019) 144–155.
[5] D. Andre, S.-J. Kim, P. Lamp, S.F. Lux, F. Maglia, O. Paschos, B. Stiaszny, J. Mater. Chem. A 3 (2015) 6709–6732.
[6] K.L. Harrison, A. Manthiram, Chem. Mater. 25 (2013) 1751–1760.
[7] M. Ren, Z. Zhou, X. Gao, L. Liu, W. Peng, J. Phys. Chem. C 112 (2008) 13043–13046.
[8] K. Saravanan, H.S. Lee, M. Kuezma, J.J. Vittal, P. Balaya, J. Mater. Chem. 21 (2011) 10042–10050.
[9] H. Zhou, Y. Shi, F. Xin, F. Omenya, M.S. Whittingham, ACS Appl. Mater. Interfaces 9 (2017) 28537–28541.
[10] T. Kerr, J. Gaubicher, L. Nazar, Electrochem. Solid-State Lett. 3 (2000) 460–462.
[11] Y. Song, P.Y. Zavalij, M.S. Whittingham, J. Electrochem. Soc. 152 (2005) A721–A728.
[12] Z. Chen, Q. Chen, L. Chen, R. Zhang, H. Zhou, N.A. Chernova, M.S. Whittingham, J. Electrochem. Soc. 160 (2013) A1777–A1780.
[13] C. Siu, I.D. Seymour, S. Britto, H. Zhang, J. Rana, J. Feng, F.O. Omenya, H. Zhou, N.A. Chernova, G. Zhou, C.P. Grey, L.F. Piper, M.S. Whittingham, Chem. Commun. 54 (2018) 7802–7805.
[14] Y. Yang, H. Fang, J. Zheng, L. Li, G. Li, G. Yan, Solid State Sci. 10 (2008) 1292–1298.
[15] C.J. Allen, Q. Jia, C. Chinnasamy, S. Mukerjee, K. Abraham, J. Electrochem. Soc. 158 (2011) A1250–A1259.
[16] M. Bianchini, J. Ateba-Mba, P. Dagault, E. Bogdan, D. Carlier, E. Suard, C. Masquelier, L. Croguennec, J. Mater. Chem. A 2 (2014) 10182–10192.
[17] Y.-C. Lin, B. Wen, K.M. Wiaderek, S. Sallis, H. Liu, S.H. Lapidus, O.J. Borkiewicz, N.F. Quackenbush, N.A. Chernova, K. Karki, F. Omenya, P.J. Chupas, L.F.J. Piper, M.S. Whittingham, K.W. Chapman, S.P. Ong, Chem. Mater. 28 (2016) 1794–1805.
[18] J. Jamnik, J. Maier, Phys. Chem. Chem. Phys. 5 (2003) 5215–5220.
[19] Y. Ren, A.R. Armstrong, F. Jiao, P.G. Bruce, J. Am. Chem. Soc. 132 (2009) 996–1004.
[20] K.T. Lee, J. Cho, Nano Today 6 (2011) 28–41.
[21] A.K. Padhi, K.S. Nanjundaswamy, J.B. Goodenough, J. Electrochem. Soc. 144 (1997) 1188–1194.
[22] Y. Shi, H. Zhou, I.D. Seymour, S. Britto, J. Rana, L.W. Wangoh, Y. Huang, Q. Yin, P.J. Reeves, M. Zuba, Y. Chung, F. Omenya, N.A. Chernova, G. Zhou, L.F.J. Piper, C.P. Grey, M.S. Whittingham, ACS Omega 3 (2018) 7310–7323.
[23] J. Rana, Y. Shi, M.J. Zuba, K.M. Wiaderek, J. Feng, H. Zhou, J. Ding, T. Wu, G. Cibin, M. Balasubramanian, F. Omenya, N.A. Chernova, K.W. Chapman, M.S. Whittingham, L.F. Piper, J. Mater. Chem. A 6 (2018) 20669–20677.
[24] M. Herrmann, U. Forter-Barth, P.B. Kempa, Cent. Eur. J. Energ. Mater. 6 (2009) 183–193.
[25] P.J. Chupas, X. Qiu, J.C. Hanson, P.L. Lee, C.P. Grey, S.J. Billinge, J. Appl. Crystallogr. 36 (2003) 1342–1347.
[26] P.J. Chupas, K.W. Chapman, P.L. Lee, J. Appl. Crystallogr. 40 (2007) 463–470.
[27] A. Hammersley, S. Svensson, M. Hanfland, A. Fitch, D. Hausermann, Int. J. High Pressure Res. 14 (1996) 235–248.
[28] B.H. Toby, R.B. Von Dreele, J. Appl. Crystallogr. 46 (2013) 544–549.
[29] P. Juhás, T. Davis, C.L. Farrow, S.J. Billinge, J. Appl. Crystallogr. 46 (2013) 560–566.
[30] C. Farrow, P. Juhas, J. Liu, D. Bryndin, E. Božin, J. Bloch, T. Proffen, S. Billinge, J. Phys. Condens. Matter 19 (2007) 335219–335225.
[31] G.A. Mabbott, J. Chem. Educ. 60 (1983) 697–702.
[32] N.M. Elgrishi, K.J. Rountree, B.D. McCarthy, E.S. Rountree, T.T. Eisenhart, J.L. Dempsey, J. Chem. Educ. 95 (2018) 197–206.
[33] C. Liu, Z.G. Neale, G. Cao, Mater. Today 19 (2016) 109–123.